

Long-term slip rate of the southern San Andreas Fault, from ^{10}Be - ^{26}Al surface exposure dating of an offset alluvial fan

Jérôme van der Woerd^{1,2*}, Yann Klinger^{3,4*}, Kerry Sieh³, Paul Tapponnier⁴,
Frederick J. Ryerson¹, Anne-Sophie Mériaux^{1,3}

(1) IGPP-LLNL, L202, 7000 East Avenue, CA94550 Livermore, USA

ryerson@llnl.gov

(2) EOST-IPGS, 5 Rue R. Descartes, 67000 Strasbourg, France

jeromev@eost.u-strasbg.fr

(3) Division of Geological and Planetary Sciences 100-23, Caltech, Pasadena, CA 91125, USA

sieh@gps.caltech.edu

(4) Laboratoire de Tectonique, IPG Paris, 4 place Jussieu, 75252 Paris Cedex 05, 75252, France

klinger@ipgp.jussieu.fr

tapponnier@ipgp.jussieu.fr

* Present address.

Abstract

The long-term slip rate of the southern San Andreas Fault in the southeastern Indio Hills appears to be only 15.9 ± 3.4 mm/a, far less than the relative motion between the Pacific and North American plates. We have determined this rate by using ^{10}Be and ^{26}Al isotopes to date an alluvial fan surface that is offset 565 ± 80 m. Twenty-six quartz-rich cobbles collected from the surface of the fan yield an age of 35.5 ± 2.5 ka. The unusually tight cluster of ages implies a simple exposure history of the fan surface and little prior exposure of clasts. The fact that the slip rate is about 30 mm/yr slower than the relative motion of the North American and Pacific plates implies that much more than half of the relative plate motion across this part of southern California has been taken up by faults other than the San Andreas over the past 35 kyr. Oddly, this slip rate is also about 10 mm/a less than recent estimates of the San Andreas' slip rate from GPS geodesy. This discrepancy may reflect temporal variations in slip rate. Alternatively, it might demonstrate that about 10 mm/a of right-lateral strain occurs on nearby secondary faults. Our study demonstrates the plausibility of obtaining better constraints on the present-day kinematics of southern California through the determination of long-term slip rates for other faults using cosmogenic dating.

How is plate motion partitioned across southern California?

The rate of horizontal translation between the Pacific and North American plates has averaged about 50 mm/a over the past 3 million years (Demets, 1995) and 48 ± 5 mm/a over the past decade (Bennett et al., 1996). Many have attempted to understand how this deformation is partitioned between the numerous active faults of southern California, because such knowledge is critical to understanding the mechanics of this complex plate boundary. These details are also important input for estimating local seismic hazards, because seismic productivity generally increases with increasing fault slip rate.

Attempts to measure the partitioning of slip across the plate boundary have relied on either short- or long-term measurements. Geodetic data enable calculation of rates spanning a few years or decades; stratigraphic, geomorphologic and geochronologic information yield rate averages that span thousands to tens of thousands of years. Heretofore, measurements of long-term slip rates have been sparse, because they depend on the presence of clearly offset landforms that can be dated by the radiocarbon method. Only at Cajon Pass and Wallace Creek (Figure 1, inset) is the millennially averaged slip rate well constrained (Weldon and Sieh, 1985; Sieh and Jahns, 1984). The rates there -- 24.5 ± 3 and 34 ± 3 mm/a, respectively -- suggest that the fault currently bears about 50 to 70 % of the entire relative plate motion.

Use of the Cajon Pass rate to establish the nature of slip partitioning farther south in southern California is probably inappropriate, because the geometry of active faults there differs greatly from their geometry at the latitude of Cajon Creek (Figure 1, inset). South of Cajon Pass, several other active strike-slip faults lie west of and sub-parallel to the San Andreas. Structural, stratigraphic and geochronologic data show that among these faults, the San Jacinto and San Andreas have long been the principal structures. Geodetic measurements show that this continues to be the case, with the two faults carrying well over half of the total relative plate motion.

The relative degree of current activity of these two faults remains controversial, however. Although the total slip across the San Andreas fault (215 km) is clearly much larger than that across the San Jacinto (20 km), some interpretations suggest that the slip rate of the San Jacinto fault over the past 30,000 years is equal to or greater than that of the San Andreas (e.g. Merifield et al., 1987; Kendrick, 2003; Matti and Morton, 1993; Bennett et al., 2004). Inversion of GPS geodetic vector fields by Bennett et al. (1996) yields best-fit slip rates of about 26 and 9 mm/a for the southern San Andreas and San Jacinto faults, respectively. These

values are from a model with the least residual errors, so other distributions of slip are possible.

More precise constraints on the millennially averaged slip rate of the San Andreas fault south of Cajon Pass would eliminate another degree of freedom in inversions of geodetic or structural data. Furthermore, a well-constrained slip rate would enable more realistic estimations of the average length of the seismic cycle. The current 300-year-long period of dormancy (Sieh, 1986; Fumal et al., 2002), for example, could be an aberration from a normal, shorter interval, or it could be typical and reflect a low rate of elastic loading.

A significant hindrance to determination of well-constrained long-term slip rates has been the difficulty of dating offset surfaces. Until recently, radiocarbon dating had been the most common and reliable means for acquiring an age. Unfortunately, carbonaceous materials are rare in offset strata, and the method is limited by the short half-life of ^{14}C to features that are younger than about 50,000 years. The development of methods to date offset geomorphic surfaces by measurement of cosmic-ray produced ^{10}Be and ^{26}Al has created new possibilities for quantifying deformation in tectonically active regions (for example, Bierman et al., 1005; Ritz et al., 1995; Repka et al., 1997; Van der Woerd et al., 1998, 2002; Mériaux et al., 2004). The value of these new methods is clear from their successful application in recent studies of the kinematics of the Indian-Asian collision. Age determinations from ^{10}Be and ^{26}Al of offset alluvial fans and glacial moraines have enabled calculation of slip rates for major strike-slip faults there. This method allows for dating of surfaces as old as about several 100,000 years and does not rely on the recovery of carbonaceous material. This raises the prospect that many hitherto undated or poorly dated offset surfaces in southern California could be dated using ^{10}Be and ^{26}Al .

The Biskra Palms site

To test this use of surface exposure dating, we focused our attention on an offset alluvial fan just southeast of Biskra Palms oasis, near the southeastern tip of the Indio Hills (Figure 1). For ease of reference, we will call this the Biskra Palms fan, even though it is in the drainage immediately southeast of the actual oasis.

Long ago Keller et al. (1982) recognized that the Biskra Palms alluvial fan (Figure 2) might enable determination of a slip rate. They estimated an offset of about 700 meters, but could not find carbonaceous materials for dating the fan surface. In lieu of radiocarbon analyses, they used the degree of soil development to estimate a 20,000- to 70,000-year age of the fan surface. Their estimated slip rate was, thus, poorly constrained between 10 and 35 mm/a, although they had reasons to favor a rate range between 23 and 35 mm/a.

We suspected that we could reduce the uncertainties in this rate determination by using cosmogenic exposure dating to reduce the uncertainties in the age estimate.

Geologic setting and mapping

The Biskra Palms fan is immediately southeast of the junction of two major strands of the San Andreas fault (Figures 1 and 2). To the southeast, the San Andreas fault continues 75 km to the Salton Sea as a relatively simple, straight structure. To the northwest, the fault divides into two principal strands, the Mission Creek and Banning faults. Offset channels and terraces between the Biskra and Thousand Palms oases indicate that the Mission Creek fault is the more active of the two near the site. The Banning fault does not traverse the site, but becomes the principal fault farther northwest (Keller et al., 1982; Yule and Sieh, 2003). Near and northwest of Biskra Palms oasis, scarps demonstrate that the Banning fault has a

significant thrust component, up on the north (Indio Hills) side. Scarps also belie the existence of many secondary faults within and along the northeastern flank of the Indio Hills (Figure 2, e.g. Powell et al., 1993). These include the Indio Hills fault, which appears to have a significant vertical component of slip. At the Biskra Palms fan, the Mission Creek fault consists of two parallel strands, 400 m apart (Figure 2). Both clearly offset the alluvial fan horizontally and vertically (Figure 3). The Biskra Palms fan was fed by a small intermittent stream that extends about 3 km into the Indio Hills (Figure 2). The stream erodes sands and gravels of the Ocotillo formation (Rogers, 1965) from a small (2.5 km^2) drainage basin.

The fan consists of a sequence of alluvial surfaces, all well preserved northwest of the modern channel until recent years (Figure 4). Quarrying operations by Granite Corporation had removed most of the younger and much of the older fan deposits by the beginning of our study in 2000 (Figure 3). Nevertheless, we were able to map the fan surfaces from old and new aerial photographs augmented by mapping in the field. To characterize the different fan surfaces and their offsets better we mapped them in the field using stereo air photos taken in both 1969 and 2004, 10-m pixel SPOT images, and SRTM digital topographic data. Several different surfaces are distinguishable on the images by the different hues that have resulted from differing degrees of development of desert pavement and varnish. The surfaces are also distinguishable by their distinct heights relative to the active streambed.

Figure 5 shows our field and remote mapping of the alluvial surfaces and faults, superimposed on the USGS 24,000-scale topographic contours and the USGS orthophoto. Cross-sections, derived from the topographic map and our field mapping, display deformation of the surfaces across the fault zone and the relative heights of the terraces (Figure 5b). Four distinct surfaces are (or were) present. From youngest to oldest, these are T0, T1, T2 and T3. Quarrying has obliterated T1 and much of, the active streambed, TO. T3 is clearly preserved

only as a solitary remnant upstream from the fault zone, although slopes between the two fault traces may also be chaotically deformed remnants of T3. T2 is the most prominent surface and the one from which we are able to determine an offset and a slip rate.

Cobbles and boulders on the T2 surface exhibit a well-developed desert varnish and pavement (Figure 6). The pavement is so well developed that very few sandy patches remain. Rounded pebbles and cobbles up to 50 cm in size are common. A discrete sublevel (T2'd) existed downstream in 1969 (Figures 4 and 5a). Unfortunately, T2'd had been completely quarried away by the time of our fieldwork. Between the two main faults, T2 is pervasively disrupted by small, oblique normal faults, oriented about 30° clockwise relative to the principal strike-slip faults (Keller et al., 1982). The normal faults crosscut abandoned drainage rills and locally offset them vertically by as much as ~10 m (Figure 5a). Only two of these faults offset the western T2 terrace riser.

The youngest inactive surface, T1, appears clearly on the 1969-vintage stereo air photos. It is lower than T2 and less incised by secondary rills. It has a lighter tone than the T2 and T3 surfaces, probably because its desert varnish is less well developed. Unfortunately, it had been almost totally removed by quarrying by 2000. Only a small patch of T1 remained, downstream from the fault zone (Figure 5a).

Offset measurements

Keller et al. (1982) recognized that the T2 surface has been offset by both strands of the fault and proposed a cumulative offset of 700 m. This value appears to an overestimate and has recently been challenged (Dorsey, 2002). Thus we discuss below in some detail the nature of the piercing lines and conclude with a reassessment of the offset measurement.

The southern strand of the Mission Creek fault is the more prominent of the two, in large part because its vertical offset across T2 and T3 is large (Figures 3, 4 and 6). In detail, the fault trace consists of a set of right-stepping traces that form an arcuate zone. Several of the gullies that incise the fault scarp are offset right-laterally. Keller et al. (1982) attributed the 50-m-high scarp to a component of reverse faulting caused by the curvature of the fault. Our observations confirm this view, and we suggest a similar interpretation on the cross-section of Figure 5b. The northern strand of the fault is more subdued and does not continue more than a couple kilometers eastward from the offset fan. To the west, it joins the main fault strand (Figure 2). It is followed locally by an ephemeral stream course, which crosses a small playa west of T2i. It accommodates mostly right-lateral motion (Figure 5b).

Both faults offset the western edge of T2. This is the only marker that enables us to quantify the offset precisely and accurately. In the following section we describe the piercing points used to assess the total right-lateral offset of T2 (Figure 5a).

First, let us consider the offset across the northern of the two fault strands. The western edge of T2u is clear north of the northern fault strand (Figures 5a). Its trend of N35E is nearly linear (Figure 7a). For most of its length however, a younger rill has eroded the western edge of T2. The bed of this small channel widens downstream, toward the northern fault. On Figure 7, piercing points A and C represent the intersections with the fault of the present eastern and western edges of this widening channel. They bracket the range of plausible piercing points for T2u. Piercing point B, between these two extremes, would represent the intersection of the western edge of T2u with the fault, if the original channel edge near the fault did not deviate from its upstream trend of N35E.

South of the northern fault strand, the western edge of T2i consists of a straight, 100-m-long, N35E-trending scarp. This scarp faces northwest, into a small valley (Figures 4 and

5a). This fan margin probably represents the largely un-eroded front of a fan delta that abutted a small lake that occupied the valley. Fine sands and silts on the valley floor attest to the former presence of a lake. This delta front intersects the northern fault at piercing point D.

The offsets between D and A, B, and C are 90, 130 and 180 m, respectively (Figure 7a). The most likely actual offset is D-B (130 m), because in this case the upstream and downstream segments of the western edge of T2 have the same strike (Figure 5b). The two other piercing points (A and C) are probably beyond the extreme lower and upper bounds for the offset, since these yield poorly matching trends for the upstream and downstream fan edges. In actuality, the upper and lower bounds for the offset of T2 across the northern strand must be closer to B than to A and C.

We turn now to an evaluation of the offset of T2 across the southern of the two fault strands. North of the southern strand, the western edge of T2i abuts a 10- to 15-m high terrace riser (Figures 3 and 5a). The riser reflects incision by the T2 stream into a pre-existing ridge of sand and gravel. Both the riser and the edge of the T2i tread are gently arcuate and collinear with that portion of the T2i tread we consider to be the front of a fan delta.

The T2i riser is cut and offset right-laterally about 30 m by a minor fault that splay off of the main fault (Figure 5a). The intersection of the T2i terrace edge and this fault are labeled E and F in Figure 7). From piercing point E the base of the terrace riser trends S78W toward the southern main fault zone, until it is cut by another minor strand of the southern fault.

Beyond this intersection, erosion has eliminated the terrace riser. Thus, one must extrapolate to the trace of the main southern strand to estimate the position of the piercing point. Linear extrapolation to the main southern strand yields a position for the piercing point at H (Figure 7a).

This piercing point may not reflect the total offset across the southern main strand, however. The arcuate nature of the terrace riser between the southern and northern strands of the fault suggests that it and terrace T2 may be right-laterally warped. The *en-échelon* field of minor faults that cuts the T2i surface also suggests that warping may have occurred (Figure 5a). However, only one of these little faults clearly offsets the terrace riser. That offset is no more than a few meters, too small to be depicted on Figure 5a. This suggests that the family of minor faults is principally a superficial feature that cuts only the thin T2i fill and not the underlying older materials. Nonetheless, these superficial faults may belie the existence of significant broad right-lateral shearing of the block between the two principal faults.

If we assume that the entire curvature of the terrace riser between the two principal fault strands is due to right-lateral warping, then we can extrapolate the N35E trend of the riser near the northern strand all the way to the southern strand to infer a piercing point at G. Since this point is about 200 m SE of piercing point H, warping could, conceivably, account for 200 m of the offset across the fault zone.

Determination of the piercing point on the southern side of the southern main strand is less complicated. The T2 fan south of the fault has a simple geometry and is cleanly offset. Five major rills incise the fan surface south of the southern main strand, including one along the fan's western margin (Figure 5A). All of these rills intersect the fault zone at a high angle and together exhibit a slightly radial pattern across the fan. The lack of any fault-parallel, dogleg segments to these channels along the fault zone suggests that these rills were abandoned soon after they formed. This, in turn, suggests that the entire existing T2 fan surface was abandoned at once.

Adjacent to the western edge of the T2d terrace is a small active stream channel. This channel is too small and services too small a drainage basin to have had the power to

significantly erode the western margin of the T2d fan. Thus the current mapped edge of the T2d fan is probably within a few meters of the original fan edge. The fan edge projects N65E into the fault zone at point J (Figure 7a).

One might argue that the original fan margin and piercing point lie farther to the west and have been overridden by the thrust fault in Figure 5A. This cannot be the case, however. First, there are no young scarps that would indicate the fault has been recently active. Second, small remnants of the T2d surface present at the mouth of tributary canyons on the hanging wall block still grade to the main T2d fan.

The distance between piercing point J and piercing points H is 405 m. Addition of the 30-m offset between points E and F yields a total offset of 435 m. If we were to allow for an extreme amount of warping by matching up piercing point J and G the offset would be 600 m. (Figure 7a).

The true offset across the southern fault zone must be close to the 435-m value, because the trends of the western edges of T2 are similar in this reconstruction. The trend of the T2 fan south of the fault zone is N65E, and the trend of the T2 terrace riser immediately north of the fault zone is N78E. Even if we allow for some rotation north of the southern fault zone, by rotating the latter so that it has a N65E trend, the offset increases only by about 40-50 m. The 600-m offset, based upon 200 meters of warping, is indefensible, because it creates an enormous mismatch between the trend of the T2 terrace riser north of the fault zone and the T2 fan south of the fault. We suggest that the uncertainty in offset across the southern main fault is no more than 50 meters or so, because of the similarity in trend of the offset features north and south of the fault zone.

Figure 7b illustrates our reconstruction of offsets across the fault zone. The reconstruction assumes that no rotation has occurred. The total offset across the fault zone is

565 m – 130 m across the northern strand and 435 m across the southern strand. Allowance for enough warp to restore the trend of the T2i terrace riser to the N65E trend of the T2d fan edge increases the total offset by about 50 m, to 615 m. Offsets across the southern fault zone much smaller than 435 m (e.g. Dorsey, 2002) must be considered unlikely, because they require piercing lines with grossly conflicting trends. Arguments that unrecognized meanders in the western margin of T2 could make smaller offsets plausible are tough to make. First, the western edge of the T2 surface is well preserved along most of its length, and there are no preserved abrupt changes in trend. Variations in its trend occur over hundreds, not tens of meters. Rills cut into T2 upstream and downstream support this inference, because they too tend to have rather uniform trends over short distances. The trends of the western margin of the T2 surface and the major rills cut into the T2 surface vary from N30E to N45E. If we allow this much variation in the piercing line where it has been obliterated by erosion near each of the two main fault zones, we derive an estimate of 80 m for the uncertainty in our measurement. In the discussion below, we take the value of 565 ± 80 m as the best estimate of the offset of the T2 surface at the site.

Cosmogenic dating

Alluvial fan and terrace surfaces, which are abandoned streambeds, may be dated with surface exposure dating techniques if deposition and incision are events of relatively short duration. Exposure of clasts to cosmic rays before deposition on a surface is largely a function of transport time and storage within the drainage basin. At Biskra Palms, the headwaters of the drainage basin are only 3 km away from the site of deposition. This suggests that inheritance related to exposure during transport is likely to be small (e.g., Van der Woerd et al., 1998). Exposure on eroding slopes may occur, however, and can be responsible for

inherited components in the total cosmogenic nuclide content (e.g. Anderson et al., 1996). This is also the case of cobbles previously deposited and then reworked and transported into the drainage basin. To detect such potential age bias we collected multiple samples from each surface (Bierman et al., 1995; Van der Woerd et al., 1998; 2000; 2002).

We dated a total of 26 quartz-rich, rooted cobbles, ranging in size from about 10 to 20 cm in diameter (Figure 6b, Table 1). Three cobbles were collected from older surfaces (two on T3u, north of the fault zone, and one on the irregular surface west of T2i; Figure 5a). From the T2 complex, we dated 20 cobbles (10 from T2u, 2 from T2i and 8 from T2d). From the youngest abandoned terrace, T1, we dated 3 cobbles (Figure 5a and Table 1). All samples came from the flattest part of the surfaces, away from recent rills. Samples locations were plotted in the field on the aerial photos, and the locations of some were determined with a handheld GPS. Positioning is essential to assess the elevation of each sample and the shielding due to surrounding relief (the Indio Hills crest line is the main shielding factor at the site). Outside small rill catchments, the flat, paved depositional surfaces show little evidence of erosion. In general, the well-preserved cobbles showed no evidence of mass wasting due to frost or fire spalling. Hence, we consider that erosion of the samples or of the surfaces occurs at a rate slow enough to be neglected.

We separated quartz and removed meteoric components using the chemical isolation method of Kohl and Nishiizumi (1992). We separated beryllium and aluminum from the dissolved quartz by anion and cation exchange chromatography, precipitated the hydroxides and ignited them to form oxides. We measured the $^{10}\text{Be}/\text{Be}$ and $^{26}\text{Al}/\text{Al}$ ratios by accelerator mass spectrometry (AMS) at the Lawrence Livermore National Laboratory AMS facility (Davis et al., 1990). Measurements were normalized to the ICN ^{10}Be and NBS ^{26}Al standards prepared by K. Nishiizumi (person. comm.).

In cases of negligible erosion and inheritance, model ages for ^{10}Be and ^{26}Al can be calculated from the expression

$$N(0,t) = (P_0 / \lambda) (1 - e^{-\lambda t}) \quad (1)$$

where $N(0,t)$ is the nuclide concentration at time t , P the surface production rate (atom.g/yr) and λ the decay constant of the nuclide (yr^{-1}). Zero-erosion model ages were calculated using a sea level-high latitude (SLHL) ^{10}Be production rate of 5.06 atoms/g-quartz/yr, based on measurements of glacial surfaces in the Sierra Nevada (Nishiizumi et al., 1989), recalculated using the revised 13,000 yr glacial retreat ages reported by Clark et al. (1995), and rescaled for latitude and altitude using the coefficients of Lal (1991), as described in Owen et al. (2002). An uncertainty of 6% on the production rate (Stone et al., 2000) is taken into account. At the latitude of our site, the variations in the geomagnetic field and pole position produce changes in the production rate. These changes can be expressed in terms of an equivalent change in geomagnetic latitude and evaluated using the data from Ohno and Hamano (1992), McEllhinny and Senanayake (1982) and the Sint-800 intensity record of Guyodo and Valet (1999). For all our samples, which are at most 1.5 km apart, we use the same latitude and longitude coordinates (33.8°N , 116.2°W) and the ages were calculated using the Stone (2000) latitude and altitude correction factors.

The isotopic concentrations and calculated model ages appear in Table 1. For all samples, save one, both ^{10}Be and ^{26}Al measurements were performed. While for most of the samples the ratio between ^{10}Be and ^{26}Al concentrations is close to 6, we observe systematically lower concentrations for ^{26}Al . We are more confident in the ^{10}Be ages because they rely on a single ratio measurement, whereas the ^{26}Al determination requires two measurements, the $^{26}\text{Al}/^{27}\text{Al}$ ratio and the ^{27}Al concentration. For these reasons, we use only the ^{10}Be data in the final age calculations, which include the geomagnetic correction (Table 1).

As such, these ages are calibrated and can be compared to dates derived from other dating methods (radiocarbon dating, for example).

South of the main fault (Figure 5a), 8 samples from T2d yield ages of 33 to 37 ka. The averaged value of these ages is 35.4 ± 1.4 , with no outliers (Figure 8). The 3 samples from T1 yield ages ranging from 11 to 37.5 ka (Figure 8). Since T1 cannot be older than T2, the oldest sample could be a reworked cobble from T2. The average age of the two youngest samples of T1, 14 ± 4 ka, is our best estimate of the age of this surface.

Between the two main faults, the average of the two cobble exposure ages obtained for T2i (33.8 and 37.1 ka) is 35.4, in good agreement with the average age of cobbles on T2d. The age of the one sample from the surface west of T2i (38.4 ka) is only slightly greater than the average age of T2.

North of the faults we can assign ages to two surfaces, T2u and T3u. Nine of the 10 samples from T2u yield ages between 31 and 40 ka, average 37.3 ± 4.4 ka, in keeping with the ages on T2i and T2d. But one sample is significantly older (45.8 ka). The two samples from T3u have ages comparable to that of T2u, even though this terrace level stands several meters higher than T2.

In summary, the age of T2 is well constrained, by 19 sample ages that cluster tightly and yield an average age of 35.5 ± 2.5 ka (Figure 8 and Table 1). The 45 Ka age of one sample from T2u is clearly an outlier and probably indicates reworking of a previously exposed clast. T1 (~14 ka) is at least 20 ka younger than T2, and might be as young as 11 ka. The age of T1 is consistent with emplacement of T1 at the end of the Last Glacial Maximum.

Long-term slip rate

We may conclude confidently that the T2 surface was emplaced 35.5 ± 2.5 kyr ago. Subsequent to that date of deposition, the surface has been offset 565 ± 80 m. Dividing this offset by this age yields an average slip rate of 15.9 ± 2.5 mm/yr at the Biskra Palms fan. This rate is lower than the geological rates determined to the north along the SAF at Cajon Pass (24.5 ± 3.5 mm/yr, Weldon and Sieh, 1985). However, as discussed below, the rate calculated here may be considered a minimum bound.

In any case, it is presently the only and best direct estimate of the rate of right-lateral displacement on the main branch of the SAF across the Indio Hills. Despite fault related deformation along the two main fault branches the reconstruction of the geometry of the northwestern limit of T2 we propose is realistic. Conservatively, we have considered a simple, almost linear, shape for this limit (Figure 7b) in agreement with the present day geomorphic characters of the surface suggested both from topographic contours and post-depositional rill incisions. Such characters require that the total offset of the T2 limit, mapped on figure 5a, must have accrued after the T2 conglomeratic fan was abandoned. Because of overlapping fan deposits downstream of the fault coupled with a component of thrusting (Figure 5a), the southeastern limit of T2 is less well defined, but overall the total offset is unlikely to be less than 500 m.

The abandonment age of T2 (35.5 ± 2.5 ka), determined from sets of samples from various parts of the surface upstream and downstream from the two fault-strands yields strong constraints on the age of the total offset of T2. The large number of surface samples (a total of 19, Figure 5a and 8), distributed over large areas of the three T2 remnants, with well clustered ages, confirm that pre-depositional exposure or post-depositional erosion were negligible and that the 35.5 ± 2.5 ka age is statistically representative of the timing of abandonment of T2. In addition, this age, which is calibrated and integrates topographic and geomagnetic corrections,

corresponds to a well-known interstadial at 35 ka, a warm pluvial separating Marine Isotope Stages 3 and 2, also described in lake sediments at Owens Lake (e.g., Bischoff and Cummins, 2001) and Mono Lake (La Joie, 1968). This would have been a period propitious to fairly rapid aggradation and fan emplacement.

While the rate we find is low, we argue that it is a minimum bound for the total slip-rate across the entire fault zone at Biskra Palms. As shown above, there is additional faulting and deformation at the site that is difficult to assess quantitatively. In particular, there are numerous N160-170 trending normal faults (Keller et al., 1982) visible across T2 and between the two major strike-slip faults (Figure 5a). A few of these faults have dextral offsets of several meters. They probably accommodate internal deformation of the block between the main faults and ought to be responsible for additional right lateral slip at the site. While motion on these faults might attest to counter-clockwise rotation of the small blocks they separate, clockwise rotation of the entire block between the two major strike-slip faults may also occur. A rotation of only 7° of this 400 m wide block would add up to 50 m to the total right-lateral offset and would increase the slip-rate by more than 10 %. Furthermore, as shown on figures 1 and 2, faults north of the most prominent strands may accommodate additional right-lateral motion in the Indio Hills. They might easily account for another 10 % increase in the slip-rate.

The major problem at Biskra Palms is to assess how the Banning Fault connects to the Mission Creek Fault and where. Clearly, the BF accommodates most of the right-lateral motion of the SAF as one moves 15 km northwest of the Indio Hills. The slip-transfer must occur within the Indio Hills, but is probably not complete at Biskra Palms. The BF becomes less and less clear as it approaches its southeastern termination, with stepping en-échelons segments that have a thrust component (Figure 2), responsible for uplift and upslope tilting of the hills southwest of the MCF. Such uplift terminates at Biskra Palms, as evidenced by the

disappearance of the hills immediately to the southeast, and no additional faulting is observed across the fans farther south.

Therefore, the actual rate could reach a value closer to that determined at Cajon Pass, north of the San Gorgonio bend along the main trace of the San Andreas fault. Such a rate would be in keeping with recent geodetic (GPS or VLBI) data that estimate the rate along the MCF to range between 21 and 28 mm/yr (Feigl et al., 1993; Bennett et al., 1996). Note that the highest rate estimate is provided by the GPS data (26 ± 2 mm/yr, Bennett et al., 1996), which integrates strain over a wide area, with the eastern most stable points being as far as 100 km away from the SAF (Bennett et al., 1996). If a few mm/yr of strain is taken up east of the Indio Hills then a better agreement between our rate and the GPS data ensues.

Alternatively, the slip-rate along the SAF from Cajon Pass to the Indio Hills might not be constant and a decrease in slip could be envisaged as the fault crosses the San Gorgonio bend. If this were the case, then some form of distributed strain transfer might occur among the different faults that make up the plate boundary. In particular, the San Jacinto Fault (SJF) might become faster and could take up as much as 10-15 mm/yr of slip, in agreement with the fastest slip estimate along it (e.g. Merifield et al., 1987; Bennett et al., 2004).

To further assess the validity of our rate within the broader, regional active deformation framework, we show on figure 9 the rates of slip on all the faults across southern California. The rates compiled are from a variety of sources and were determined by different methods (e.g., Wesnousky, 1986; Peterson and Wesnousky, 1994; Jennings, 1994; Dolan and Pratt, 1997; McGill and Sieh, 1993). When possible we show geologically determined rates, which provide information over comparable time spans. Considering the total slip budget across the plate boundary along three different paths (1-3, Figure 9), we obtain similar values of about 40-47 mm/yr. This first order calculation likely underestimates the total motion of the Pacific plate relative to North America, which probably explains the difference with the

Nuvel-1A predictions of 45-55 mm/yr (Demets, 1995; Figure 9). If one considers that the total rates across the three paths have to be the same, then the rate we determine at Biskra Palms suggests that the San Jacinto fault moves fast (10-15 mm/yr, i.e. 20-30 % of the plate motion).

Conclusion

The slip rate we obtain at Biskra Palms using cosmogenic dating (15.9 ± 2.5 mm/yr) spans a 35,000 years period, yielding information about 20 ka farther back in time than at any other location along the SAF. It places a strong new constraint on slip distribution amongst the faults of southern California.

To a first order, this rate is slower than even the lower bounds of the geological rate at Cajon Pass, 24.5 ± 3.5 mm/yr (Weldon and Sieh, 1985), and of the VLBI (Feigl et al., 1993) and GPS (Bennett et al., 1996) rates of 26 ± 2 mm/yr and 23 ± 2 mm/yr, respectively. Yet, it confirms that near Indio, the MCF is the principal strand of the SAF, accommodating most (35%) of the relative motion between the Pacific and North American plates. The relatively slow rate on the main branch of the SAF at Biskra Palms suggests that the slip rate on the San Jacinto Fault maybe closer to the upper bounds of rates determined along this fault (10-15 mm/yr). Because it remains on the low side of all other rates determined on the southern SAF, we suspect that it is a minimum bound. This inference is supported by the fact that we obtain this rate at a rather complex location where the SAF splits into two branches (BF and MCF), with a significant change in strike ($\sim 10^\circ$ towards west). Some motion must be accommodated by thrusting at Biskra Palms, and probably some more by adjacent normal faults. Also, the rates at Cajon Pass and Biskra, on either side of the San Gorgonio restraining bend, need not be precisely the same, if diffuse strain transfer occurs across the San Bernardino and San Jacinto mountains (e.g., Spotila et al., 1998; Kendrick et al., 2002). Finally, space geodesy

rates span only the last 15 years and, as observed elsewhere (e.g. Peltzer et al., 2001), millennial slip rates, especially spanning as much as 35,000 years, need not be identical if strain build-up varies through the seismic cycle and on larger time-scales (Bennett et al., 2004; Friedrich et al., 2003).

Clearly, our study at Biskra Palms is only a first step towards documenting late Pleistocene slip rates in southern California. To determine how strain was actually distributed within the Plate Boundary system in the last few tens of thousands of years, many other localities along the different faults of southern California will have to be targeted for cosmogenic dating.

Acknowledgments

We thank R.C. Finkel and M.W. Caffee at Lawrence Livermore National Laboratory for their help in analyzing the samples. Special thanks to Granite Corporation for allowing unlimited access to the fans, and especially to Lola Green and Lilburn Corporation for sharing topographic data. Tom Rockwell was kind to take one of us in his plane to fly over the Indio Hills. This work benefited funding from Lawrence Livermore National Laboratory #xx This research was supported in part by the Gordon and Betty Moore Foundation. This is Caltech Tectonic Observatory Contribution #9.

References

- Allen, C.R. (1957), San Andreas fault zone in San Gorgonio Pass, southern California, *Bull. Geol. Soc. Am.*, 68, 315-350.
- Anderson, R.S., J.L. Repka and G.S. Dick (1996), Explicit treatment of inheritance in dating depositional surfaces using in situ ^{10}Be and ^{26}Al , *Geology*, 24, 47-51.
- Bennett, R.A., W. Rodi, and R.E. Reilinger (1996), Global Positioning System constraints on fault slip rates in southern California and northern Baja, Mexico, *J. Geophys. Res.*, 101, 21,943-21,960.
- Bennett, R.A., A.M. Friedrich, K.P. Furlong (2004), Codependent histories of the San Andreas and San Jacinto fault zones from inversion of fault displacement rates, *Geology*, 32, 961-964, doi: 10.1130/G20806.1.
- Bierman, P.R., A.R. Gillespie and M.W. Caffee (1995), Cosmogenic ages for earthquake recurrence interval and debris flow fan deposition, Owens Valley, California, *Science*, 270, 447-450.

Bischoff, J.L., and K. Cummins (2001), Wisconsin glaciation of the Sierra Nevada (79,000-15,000 yr B.P.) as recorded by rock flour in sediments of Owens Lake, California, *Quaternary Research*, 55, 14-24.

Clark, M.M. (1984), Map showing recently active breaks along the San Andreas fault and associated faults between Salton Sea and Whitewater River-Mission Creek, California, U.S. Geological Survey Miscellaneous Investigations Map I-1483, scale 1:24,000.

Clark, D.H., P.R. Bierman and P. Larsen (1995), Improving in-situ cosmogenic chronometers, *Quaternary Research*, 44, 367-377.

Davis, J.C., Proctor, I.D., Southon, J.R., Caffee, M.W., Heikkinen, D.W., Roberts, M.L., Turteltaub, K.W., Nelson, D.E., Loyd, D.H. and Vogel, J.S. (1990), LLNL/UC AMS facility and research program: Nuclear instruments and methods in Physics Research, *B52*, 269-272.

Demets, C., R.G. Gordon, D.F. Argus and S. Stein (1990), Current plate motions, *Geophys. J. Int.*, 101, 425-478.

Demets, C., R.G. Gordon, D.F. Argus and S. Stein (1994), Effects of recent revisions to the geomagnetic reversal time scale on estimates of current plate motions, *Geophys. Res. Lett.*, 21, 2191-2194.

Demets, C. (1995), Reappraisal of seafloor spreading lineations in the Gulf of California: Implications for the transfer of Baja California to the Pacific plate and estimates of Pacific-North America motion, *Geophys. Res. Lett.*, 22, 3545-3548.

Dolan, J.F., and Pratt T.L. (1997), High-resolution seismic reflection profiling of the Santa Monica Fault Zone, West Los Angeles, California, *Geophys. Res. Lett.*, 24, 2051-2054.

Dorsey, B. (2002), Late Pleistocene slip-rate on the Coachella Valley segment of the San Andreas fault and implications for regional slip partitioning, abstract, Cordilleran Section GSA 99th Annual Meeting, April 1-3, 2003, Puerto Vallarta, Jalisco, Mexico.

Feigl, K.L. et al. (1993), Space geodetic measurement of crustal deformation in central and southern California, 1984-1992, *J. Geophys. Res.*, 98, 21,677-21,712.

Friedrich, A. M., B. P. Wernicke, N. A. Niemi, R. A. Bennett, and J. L. Davis (2003), Comparison of geodetic and geologic data from the Wasatch region, Utah, and implications for the spectral character of Earth deformation at periods of 10 to 10 million years, *J. Geophys. Res.*, 108 (B4), 2199, doi:10.1029/2001JB000682.

Fumal, T.E., M.J. Rymer, and G.G. Seitz (2002), Timing of large earthquakes since AD 800 on the Mission Creek strand of the San Andreas fault zone at Thousand Palms Oasis, near Palm Springs, California, *Bull. Seism. Soc. Am.*, 92, 2841-2860.

Guyodo, Y., and J.P. Valet (1999), Global changes in intensity of the Earth's magnetic field during the past 800 kyr, *Nature*, 399, 249-252.

Keller, E.A., M.S. Bonkowski, R.J. Korsch, R.J. Shlemon (1982), Tectonic geomorphology of the San Andreas fault zone in the southern Indio Hills, Coachella Valley, California, *Geol. Soc. Am. Bull.*, 93, 46-56.

Kendrick, K.J., D.M. Morton, S.G. Wells, R.W. Simpson (2002), Spatial and temporal deformation along the northern San Jacinto fault, southern California: Implications for slip rates, *Bull. Seism. Soc. Am.*, 92, 2782-2802.

Kohl, C.P. and K. Nishiizumi (1992), Chemical isolation of quartz for measurement of in-situ produced cosmogenic nuclides, *Geochim. Cosmochim. Acta*, 56, 3583-3587.

LaJoie, K. R. (1968), Quaternary stratigraphy and geologic history of Mono Basin, Eastern California, thesis, Ph.D., Department of Geology and Geophysics, University of California, Berkeley, California, USA.

Lal, D. (1991), Cosmic ray labeling of erosion surfaces: In situ production rates and erosion models, *Earth Planet. Sci. Lett.*, 104, 424-439.

Matti, J.C., and Morton, D.M. (1993), Paleogeographic evolution of the San Andreas fault insouthern California: A reconstruction based on a new cross-fault correlation, in *The San Andreas Fault System: Displacement, Palinspastic Reconstruction, and Geologic Evolution*, Powell, R.E., Weldon, R.J., and Matti, J.C., eds., *Geol. Soc. Am. Memoir*, 178, 107-159.

McGill, S., and K. Sieh (1993), Holocene slip rate of the central Garlock Fault in southeastern Searles valley, California, *J. Geophys. Res.*, 98, 14,217-14,231.

McElhinny, M.W., and W.E. Senanayake (1982), Variations in the geomagnetic dipole 1: the past 50,000 years, *J. Geomag. Geoelec.*, 34, 39-51.

Merifield, P.M., T.K. Rockwell, and C.C. Loughman (1987), Slip rate on the San Jacinto fault zone in the Anza seismic gap, southern California, *Geol. Soc. of Am. Abst. with Progs.*, 19, 431.

Nishiizumi, K., E.L. Winterer, C.P. Kohl, J. Klein, R. Middleton, D. Lal, and J.R. Arnold (1989), Cosmic ray production rates of ^{10}Be and ^{26}Al in quartz from glacially polished rocks, *J. Geophys. Res.*, 94 (B12), 17907-17915.

Ohno, M., and Y. Hamano (1992), Geomagnetic poles over the past 10,000 years, *Geophys. Res. Lett.*, 19, 1715-1718.

Peltzer, G., F. Crampe, S. Hensley, P. Rosen (2001), Transient strain accumulation and fault interaction in the Eastern California shear zone, *Geology*, 29, 975-978.

Petersen, M.D., and S.G. Wesnousky (1994), Fault slip rates and earthquake histories for active faults in southern California, *Bull. Seismol. Soc. Am.*, 84, 1608-1649.

Powel, R.E., R.J. Weldon, and J.C. Matti (1993), The San Andreas Fault system: Displacement, palinspastic reconstruction, and geologic evolution, *Geol. Soc. Am. Memoir*, 178, 332 p.

- Repka, J.L., R.S. Anderson and R.C. Finkel (1997), Cosmogenic dating of fluvial terraces, Fremont River, Utah, *Earth Planet. Sci. Lett.*, 152, 59-73.
- Ritz, J.F., E.T. Brown, D.L. Bourlès, H. Phillip, A. Schlupp, V.M. Raisbeck, F. You and B. Enkhtuvshin (1995), Slip rates along active faults estimated with cosmic-ray-exposure dates: Application to the Bogd fault, Gobi-Altaï, Mongolia, *Geology*, 23, 1019-1022.
- Rockwell , T., C. Loughman, and P. Merifield (1990), Late Quaternary rate of slip along the San Jacinto fault zone near Anza, Southern California, *J. Geophys. Res.*, 95, 8593-8605.
- Rogers, T.H. (1965), Geologic Map of California, Santa Ana Sheet, fifth printing 1985, Olaf P. Jenkins edition, California Division of Mines and Geology.
- Salyards, S.L., Sieh, K.E., and Kirschvink, J.L. (1992), Paleomagnetic measurements of non-brITTLE deformation across the San Andreas fault at Pallett Creek, *J. Geophys. Res.*, 97, 12,457–12,470.
- Sharp, R.V. (1981), Variables rates of late Quaternary strike-slip on the San Jacinto fault zone, southern California, *J. Geophys. Res.*, 86, 1754-1762.
- Sieh, K., and R. Jahns (1984), Holocene activity of the San Andreas fault at Wallace Creek, California, *Geol. Soc. Am. Bull.*, 95, 883-896.
- Sieh, K. (1986), Slip rate across the San Andreas fault and prehistoric earthquakes at Indio, California, *Eos Trans. AGU*, 67, 1200.
- Spotila, J.A., K.A. Farley, K. Sieh (1998), Uplift and erosion of the San Bernardino Mountains associated with transpression along the San Andreas fault, California, as constrained by radiogenic helium thermochronometry, *Tectonics*, 17, 360-378.
- Stone, J.O. (2000), Air pressure and cosmogenic isotope production, *J. Geophys. Res.*, 105, 23,753-23,759.
- Van der Woerd, J., F.J. Ryerson, P. Tapponnier, Y. Gaudemer, R. Finkel, A.S. Mériaux, M. Caffee, Zhao Guoguang, and He Qunlu (1998), Holocene left slip-rate determined by

cosmogenic surface dating on the Xidatan segment of the Kunlun Fault (Qinghai, China), *Geology*, 26, 695-698.

Van der Woerd, J., P. Tapponnier, F.J. Ryerson, A.S. Mériaux, B. Meyer, Y. Gaudemer, R.C. Finkel, M.W. Caffee, Zhao Guoguang, and Xu Zhiqin (2002), Uniform postglacial slip-rate along the central 600 km of the Kunlun Fault (Tibet), from ^{26}Al , ^{10}Be and ^{14}C dating of riser offsets, and climatic origin of the regional morphology, *Geophys. J. Int.*, 148, 356-388.

Weldon, R.J., and K.E. Sieh (1985), Holocene rate of slip and tentative recurrence interval for large earthquakes on the San Andreas fault, Cajon Pass, southern California, *Geol. Soc. Am. Bull.*, 96, 793-812.

Weldon, R.J. and E. Humphreys (1986), A kinematic model of southern California, *Tectonics*, 5, 33-48.

Wesnousky, S.G. (1986), Earthquakes, Quaternary faults, and seismic hazards in California, *J. Geophys. Res.*, 91, 12,587-12,631.

Williams, P.L. (1989), Aspects of the earthquake geology and seismotectonics of the southern San Andreas and relatd fault, southern California, Thesis, Ph.D., Columbia University, New York, USA.

Yule, D., and K. Sieh (2003), Complexities of the San Andreas fault near San Gorgonio Pass: Implications for large earthquakes, *J. Geophys. Res.*, 108, 2548, doi:10.1029/2001JB000451.

Table 1. ^{10}Be and ^{26}Al nuclide concentrations for 26 surface samples from different alluvial surfaces at Biskra Palms site. ^{10}Be age is calculated with corresponding geographic and topographic correction factors (see text for details). Average age and standard deviation are calculated for each surface. Star indicates sample not included in average calculation.

Figure captions

Figure 1: Map of San Andreas Fault system in the Coachella Valley. Biskra Palms site is located along southwestern Indio Hills, just southeast of the Biskra Palms oasis. Background is shaded DEM derived from Shuttle Radar Topography Mission data (30m pixel). Inset, modified from Weldon and Humphreys (1986), shows Biskra Palms site in relation to other sites where geological long-term slip-rate have been already determined. Green arrows (Weldon and Humphreys, 1986) indicate relative motion of various crustal blocks relative to North American plate (SCF: San Clemente Fault; EF: Elsinore Fault; SJF: San Jacinto Fault; SAF: San Andreas Fault; GF: Garlock Fault; PMF: Pinto Mountain Fault).

Figure 2: a) SPOT image of the southeastern Indio Hills. Main trace of San Andreas fault is visible across uplifted and dissected alluvial sands and gravels of the Indio Hills. Streams that cross the main fault trace have jogs that are characteristic of right-lateral motion along the fault. b) Schematic interpretation of fault traces and main alluvial units visible on the image. TPC: Thousand Palms Canyon; PC: Pushawalla Canyon; BPO: Biskra Palms Oasis). SPOT image is KJ 545-282, taken 13 November 1999.

Figure 3: Oblique aerial view of the Biskra Palms fan surface, offset by two strands of the Mission Creek fault. By the time the photo was taken, in 2002, most of the fan downstream from the principal strand of the fault had been removed by quarrying.

Figure 4: Vertical aerial photo of Biskra Palms site. Main fan surface T2d, south of the fault, has been disconnected from its upstream counterparts T2i and T2u, by right-lateral motion along the fault. Youngest alluvial surfaces are T0. T1d is an intermediate terrace.

Figure 5: a) Map of fault traces and alluvial surfaces superimposed on topographic contours and orthophoto. Numbered yellow dots show locations of samples collected for cosmogenic dating. Straight lines indicate positions of topographic profiles superimposed in Figure 5b. b) Superimposed topographic profiles across main alluvial levels, projected to a line perpendicular to strike of the fault zone. Match between surfaces northeast and southwest of central fault zone is clear. Main scarp along the principal strike-slip fault is likely due to thrust component and uplift of block between the two strike-slip faults. Fault geometry at depth, though hypothetical, is consistent with this interpretation.

Figure 6: a) The surface of terrace T2d, downstream of the fault zone. View to northeast, towards principal fault zone marked by aligned palm trees and by scarp. Lightly varnished cobbles paving the alluvial surface are typical of those sampled for surface exposure dating. b) Close-up of desert pavement on T2u surface northeast of fault. The white cobble near the head of the rock hammer is sample # 18 (^{10}Be age of 35.4 ± 3.9 ka).

Figure 7: a) Map of alluvial unit T2, faults and various considered piercing points. Blue dotted lines are western edges of T2 that we consider for offset estimation. Lettered circles are piercing points defined by intersection of dotted lines with fault traces. b) Preferred reconstruction of T2 surface and corresponding total offset values.

Figure 8: Plot of ^{10}Be model ages for each surface. The positions of each principal fault strand relative to the surfaces appear as vertical lines. Dashed line represents average age for T2. Grey stripe is average standard deviation for samples represented by squares. Data are tabulated in Table 1.

Figure 9: Map of Southern California active faults. Green arrow is motion vector of Pacific plate relative to North America with bounds in mm/yr of relative motion from Nuvel-1A model (Demets et al., 1995). Values for slip-rates on various faults and sites along SAF are from the literature (see text for references). Rates are expressed for right-lateral slip in mm/yr, except for GFZ and PMF, which are left-lateral faults. New rate at Biskra Palms is from this study. Blue dotted lines 1, 2 and 3 are paths along which we summed slip-rates across plate boundary. WC: Wallace Creek; PC: Palett Creek; CP: Cajon Pass; OVFZ: Owens Valley Fault Zone; PVFZ: Panamint Valley Fault Zone; DVFZ: Death Valley Fault Zone; BF: Blackwater Fault; BUF: Bullion Fault; CFZ: Calico Fault Zone; EMF: Emerson Fault; PMF: Pinto Mountain Fault; SGP: San Gorgonio Pass; IFZ: Imperial Fault Zone; CPF: Cerro Prieto Fault; SJF: San Jacinto Fault; EF: Elsinore Fault; NIFZ: Newport-Inglewood Fault Zone; CBFZ: Coronado Bank Fault Zone; SDTFZ: San DiegoTrough Fault Zone; SCF: San Clemente Fault.

Table 1. ^{10}Be and ^{26}Al nuclide concentration for 26 surface samples of different alluvial surfaces at the Biskra Palms site.

Sample number	Elevation (m a.s.l.)	^{10}Be 10e4 at.g-1	^{26}Al 10e4 at.g-1	$^{26}\text{Al}/^{10}\text{Be}$	lat/alt correction	depth/top correction	^{10}Be age	Mean terrace Age§ (years)
Terrace T3u								
9	170	14.544 ± 2.079	87.769 ± 11.783	6.03	1.0076	0.9549	30.7 ± 4.47	
10	170	17.169 ± 2.001	80.138 ± 9.414	4.67	1.0076	0.9549	35.96 ± 4.31	33.33 ± 3.72
Terrace T2u								
13	165	19.026 ± 1.892	87.789 ± 11.432	4.61	1.0034	0.9550	39.66 ± 4.1	
14	165	18.453 ± 2.238	114.348 ± 14.083	6.20	1.0034	0.9550	38.55 ± 4.8	
17	155	21.943 ± 1.925	109.06 ± 12.482	4.97	0.9950	0.9555	$45.81 \pm 4.22^*$	
18	155	16.66 ± 1.788	81.015 ± 9.528	4.86	0.9950	0.9555	35.37 ± 3.92	
19	150	14.449 ± 1.674	76.224 ± 9.451	5.28	0.9909	0.9554	30.98 ± 3.7	
20	150	19.035 ± 1.964	89.438 ± 10.576	4.70	0.9909	0.9555	40.13 ± 4.29	
21	150	19.246 ± 1.273	84.108 ± 10.157	4.37	0.9909	0.9554	40.54 ± 2.92	
22	150	15.624 ± 1.131	75.772 ± 9.028	4.85	0.9909	0.9555	33.4 ± 2.6	
23	150	15.353 ± 1.117	86.771 ± 11.62	5.65	0.9909	0.9555	32.84 ± 2.56	
24	150	17.133 ± 1.204	73.357 ± 12.197	4.28	0.9909	0.9555	36.44 ± 2.76	37.37 ± 4.44
Terrace T3i								
28	150	18.179 ± 1.314	73.916 ± 19.572	4.07	0.9909	0.9558	38.45 ± 2.98	38.45 ± 2.98
Terrace T2i								
29	140	17.35 ± 1.2	86.018 ± 10.346	4.96	0.9825	0.9558	37.13 ± 2.77	
30	140	15.679 ± 1.181	80.765 ± 10.841	5.15	0.9825	0.9558	33.78 ± 2.72	35.45 ± 2.37
Terrace T2d								
1	84	15.287 ± 0.561	84.65 ± 9.573	5.54	0.9367	0.9533	34.6 ± 1.6	
3	84	16.378 ± 0.586	102.963 ± 7.337	6.29	0.9367	0.9533	36.9 ± 1.68	
7	75	15.639 ± 0.547	91.353 ± 11.1	5.84	0.9295	0.9533	35.62 ± 1.6	
2	84	14.561 ± 1.702	91.357 ± 7.346	6.27	0.9367	0.9534	33.02 ± 3.97	
4	84	16.11 ± 1.857			0.9367	0.9534	36.34 ± 4.31	
5	84	16.315 ± 1.874	82.935 ± 6.668	5.08	0.9367	0.9533	36.77 ± 4.35	
6	80	15.919 ± 2.582	81.591 ± 8.387	5.13	0.9335	0.9533	36.06 ± 5.94	
8	75	14.984 ± 1.871	75.843 ± 14.617	5.06	0.9295	0.9534	34.2 ± 4.38	35.44 ± 1.37
Terrace T1								
50	30	7.253 ± 0.265	63.346 ± 7.857	8.73	0.8938	0.9534	17.52 ± 0.81	
51	30	4.576 ± 0.184	31.98 ± 5.048	6.99	0.8938	0.9532	11.08 ± 0.54	14.30 ± 4.56
52	30	15.679 ± 0.503	117.253 ± 14.841	7.48	0.8938	0.9534	37.02 ± 1.58	
Average = 5.48 ± 1.07								
Average T2 35.53 ± 2.48								

§ Mean is average of ^{10}Be age, and error is standard deviation.

* Not included in average calculation.

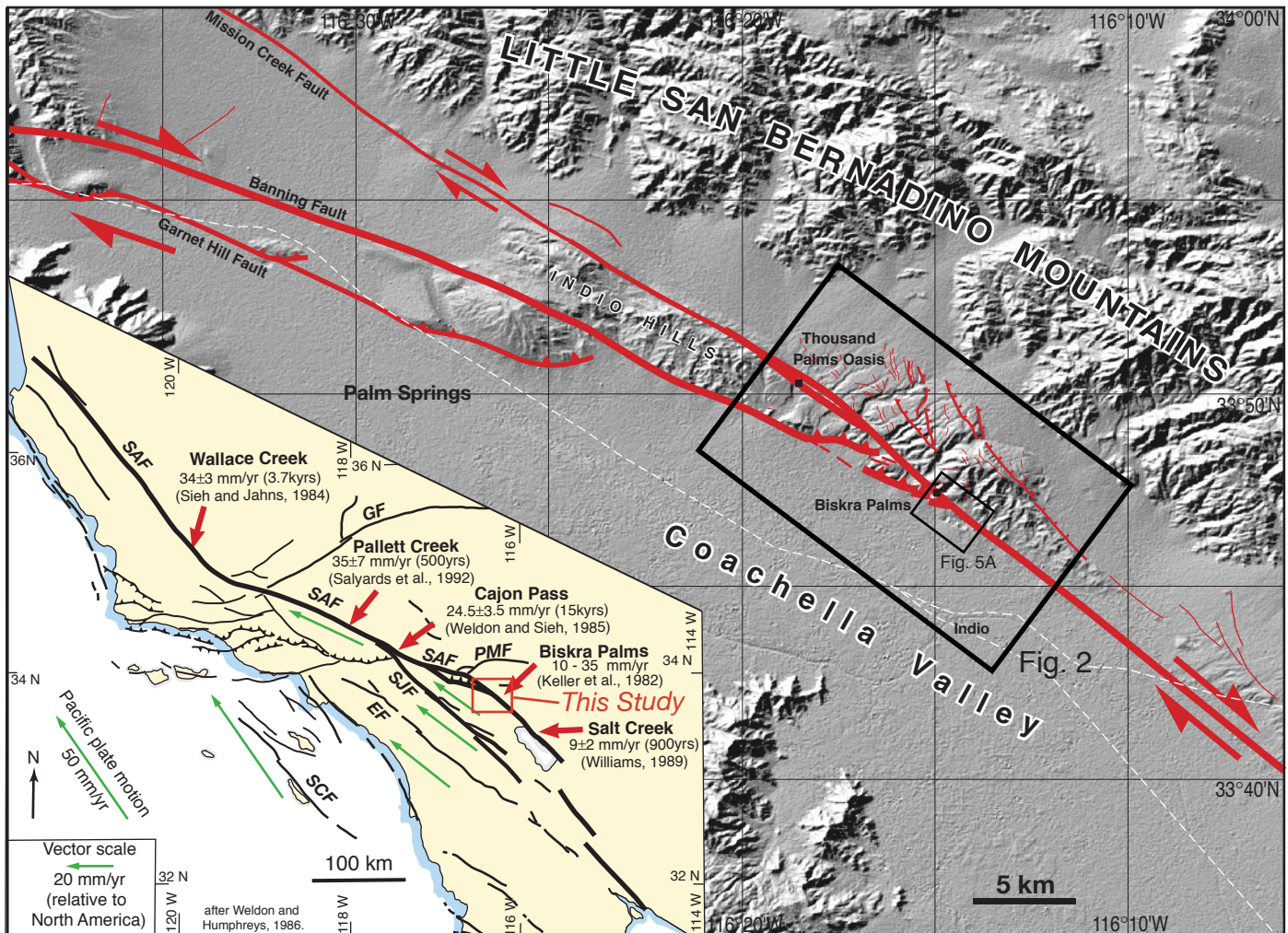


Figure 1

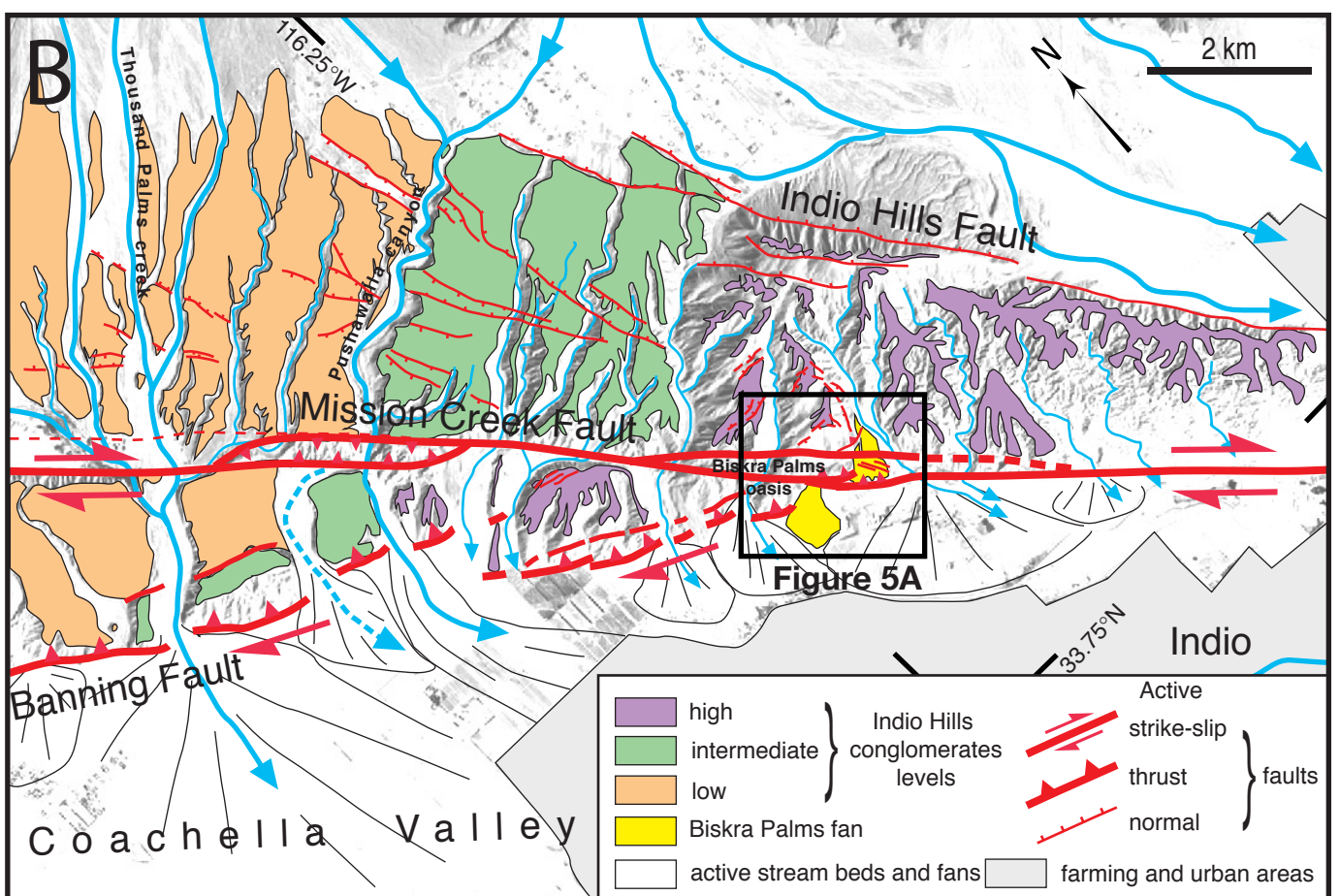


Figure 2



Figure 3

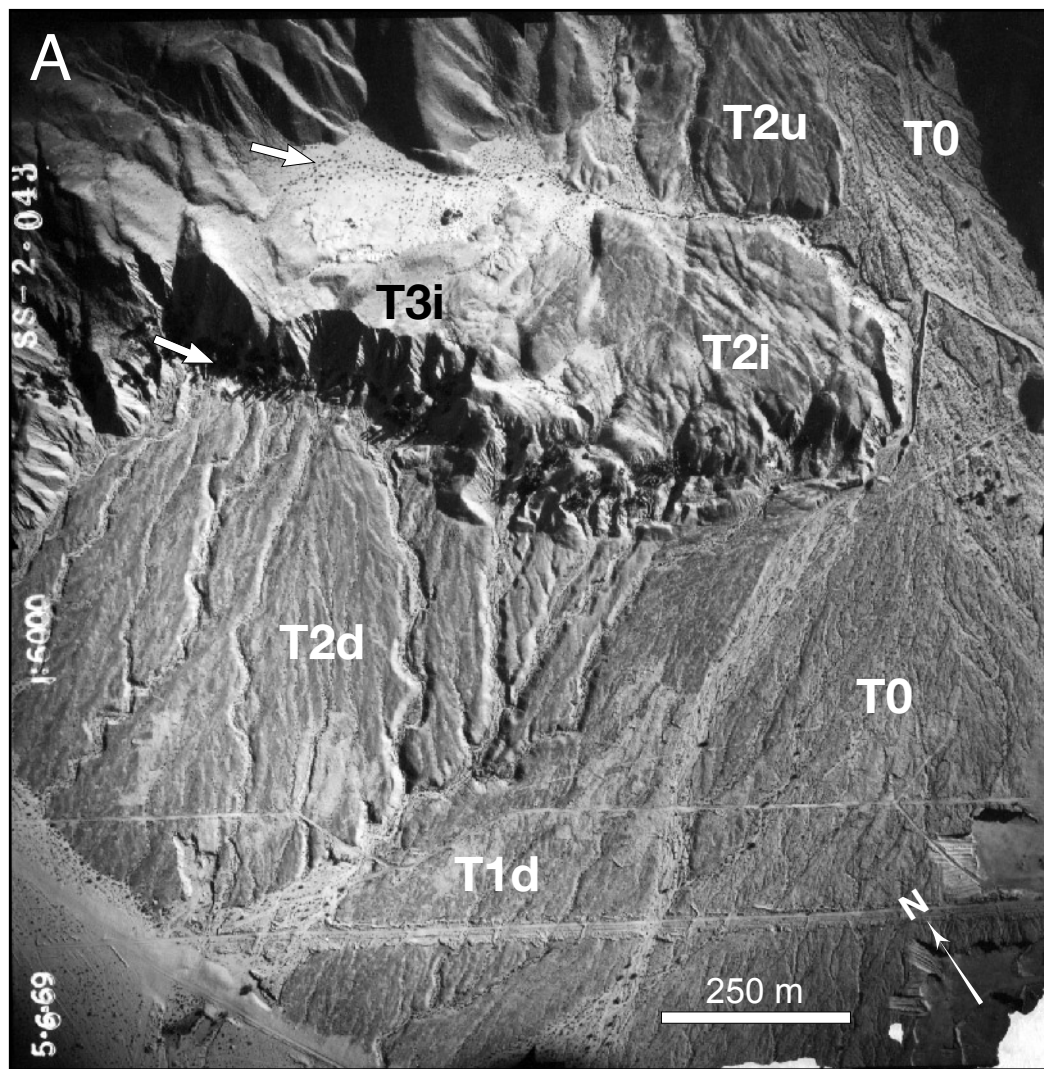


Figure 4

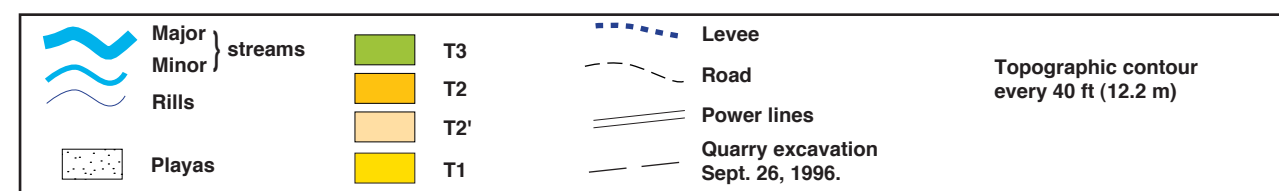
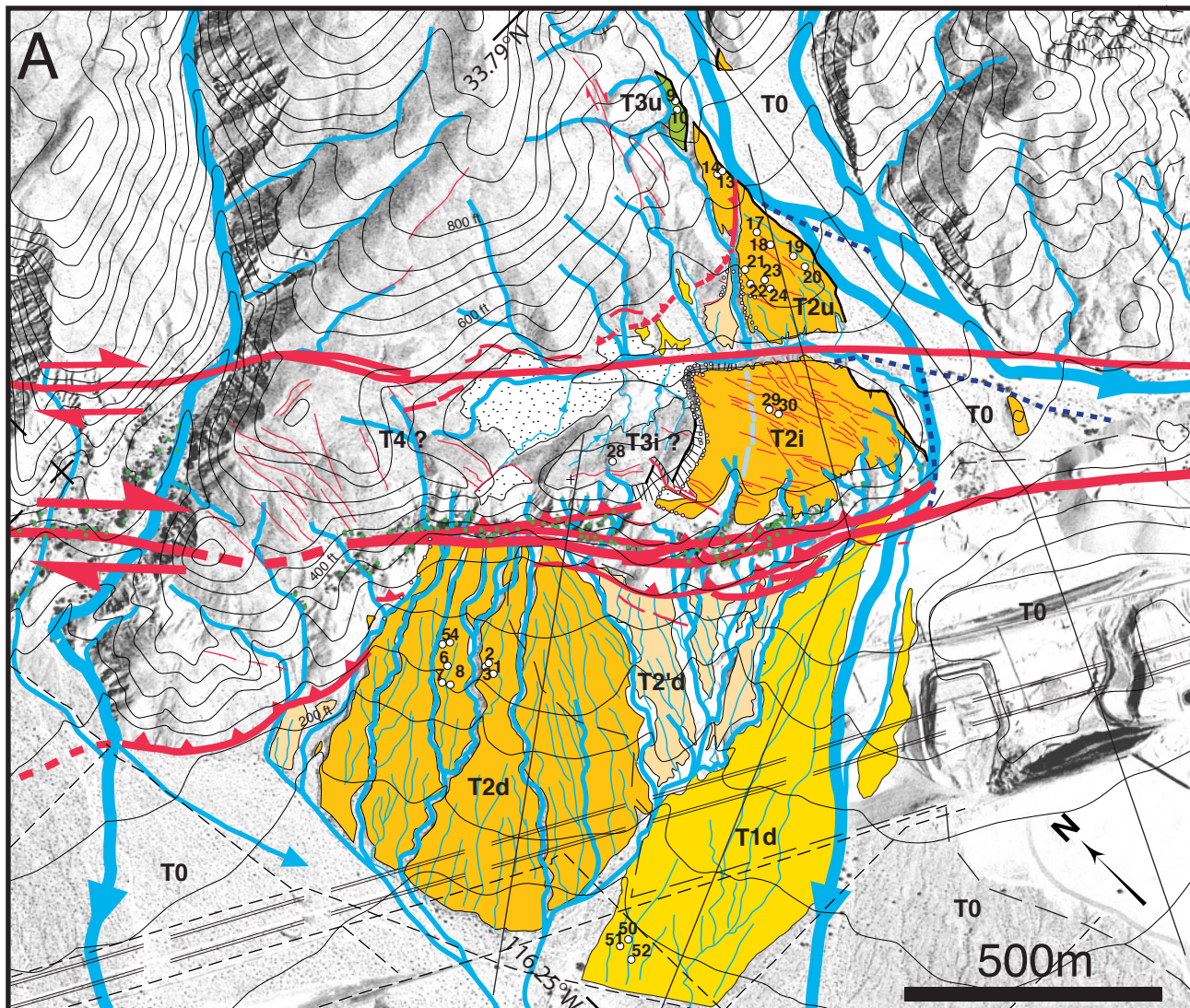
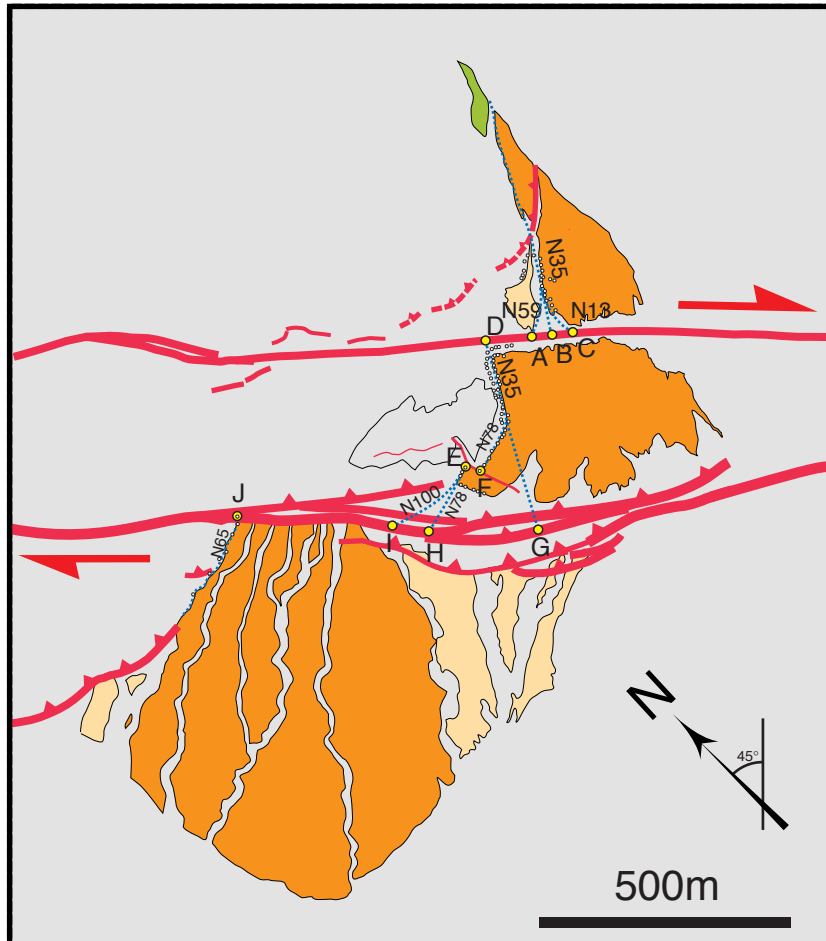


Figure 5AB



Figure 6

A



B

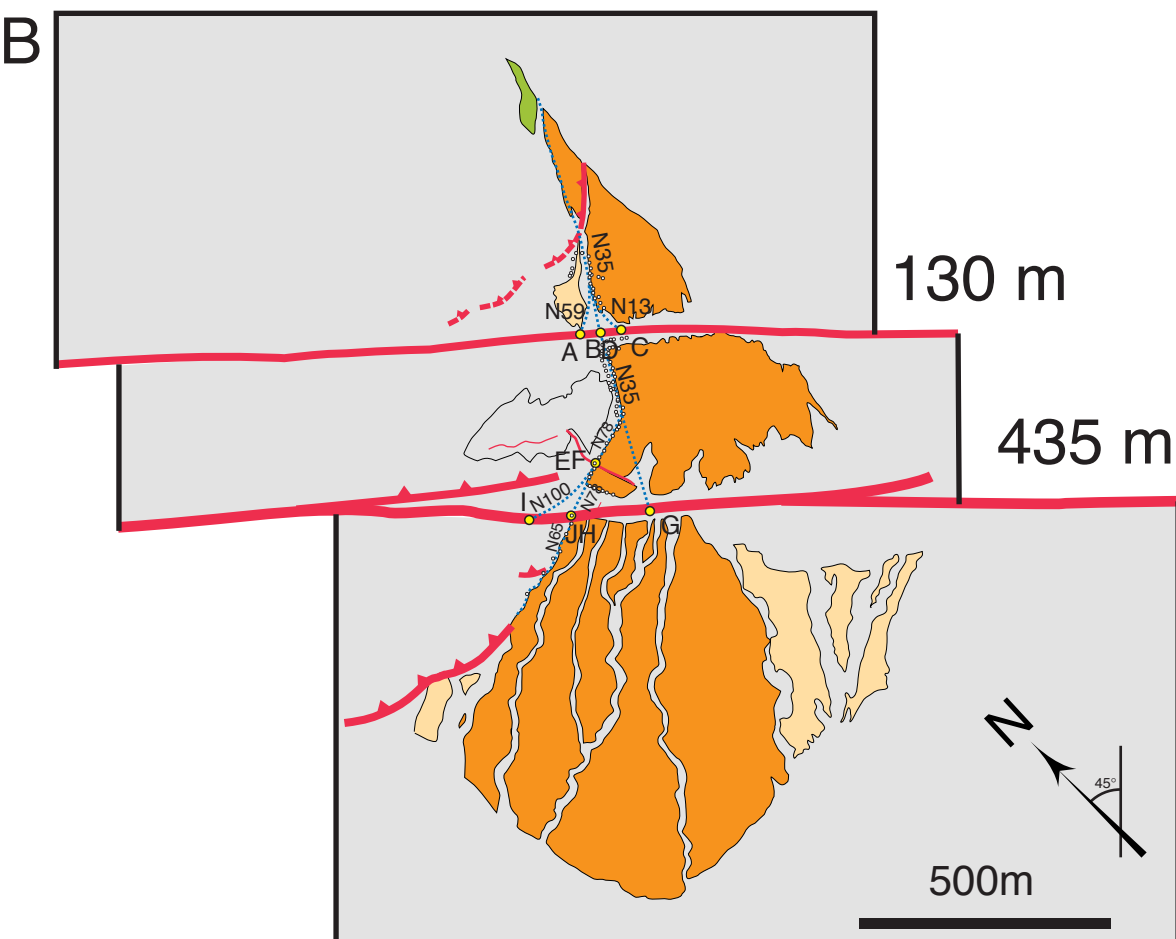


Figure 7AB

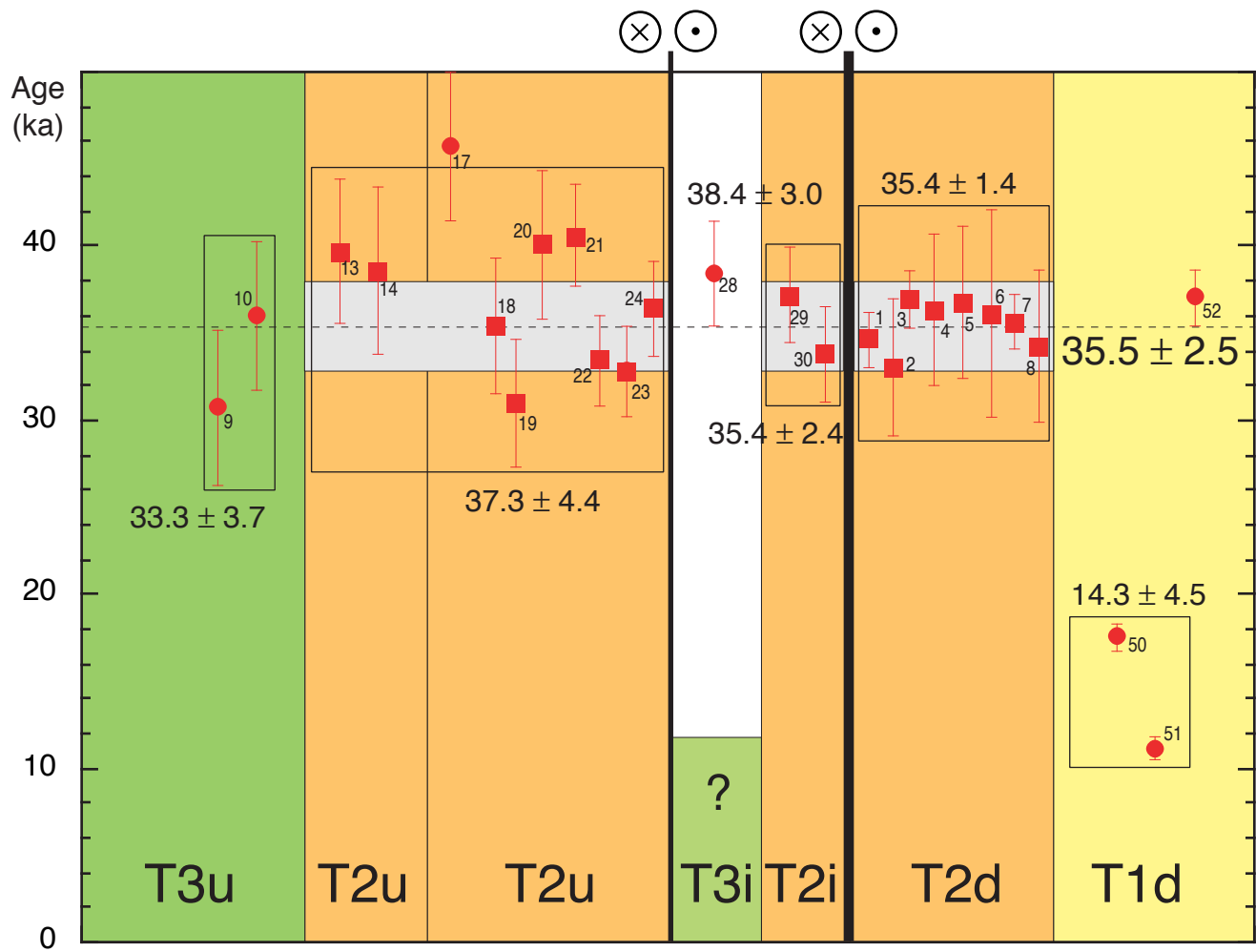
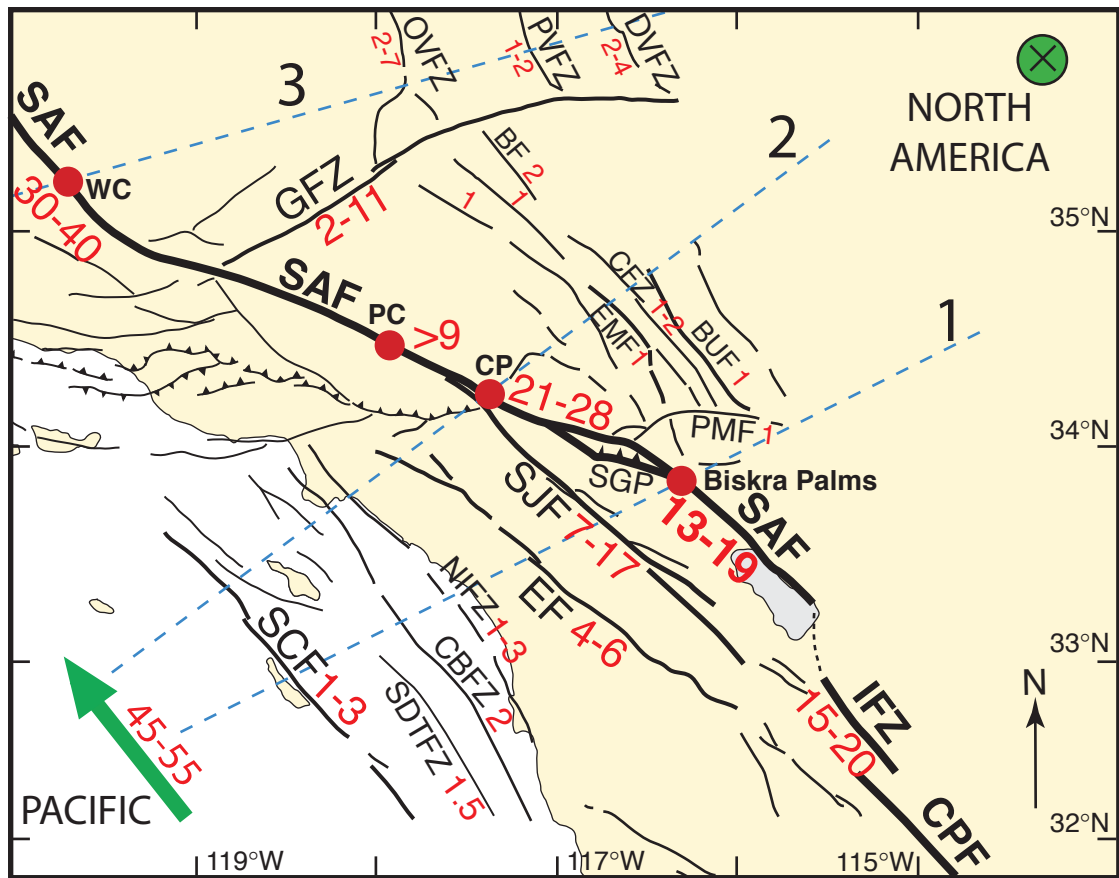


Figure 8



$$1 = (1-3)+1.5+2+(1-3)+(4-6)+(7-17)+(13-19) = 40.2 \pm 6.1 \text{ mm/yr}$$

$$2 = (1-3)+1.5+2+(1-3)+(4-6)+(7-17)+(21-28)+1+(1-2)+1 = 47.5 \pm 6.4 \text{ mm/yr}$$

$$3 = (30-40)+(2-7)+(1-2)+(2-4) = 44 \pm 5.7 \text{ mm/yr}$$

Figure 9

Table 1. ^{10}Be and ^{26}Al nuclide concentration for 26 surface samples of different alluvial surfaces at the Biskra Palms site.

Sample number	Elevation (m a.s.l.)	^{10}Be 10e4 at.g-1	^{26}Al 10e4 at.g-1	$^{26}\text{Al}/^{10}\text{Be}$	lat/alt correction	depth/top correction	^{10}Be age	Mean terrace Age§ (years)
Terrace T3u								
9	170	14.544 ± 2.079	87.769 ± 11.783	6.03	1.0076	0.9549	30.7 ± 4.47	
10	170	17.169 ± 2.001	80.138 ± 9.414	4.67	1.0076	0.9549	35.96 ± 4.31	33.33 ± 3.72
Terrace T2u								
13	165	19.026 ± 1.892	87.789 ± 11.432	4.61	1.0034	0.9550	39.66 ± 4.1	
14	165	18.453 ± 2.238	114.348 ± 14.083	6.20	1.0034	0.9550	38.55 ± 4.8	
17	155	21.943 ± 1.925	109.06 ± 12.482	4.97	0.9950	0.9555	$45.81 \pm 4.22^*$	
18	155	16.66 ± 1.788	81.015 ± 9.528	4.86	0.9950	0.9555	35.37 ± 3.92	
19	150	14.449 ± 1.674	76.224 ± 9.451	5.28	0.9909	0.9554	30.98 ± 3.7	
20	150	19.035 ± 1.964	89.438 ± 10.576	4.70	0.9909	0.9555	40.13 ± 4.29	
21	150	19.246 ± 1.273	84.108 ± 10.157	4.37	0.9909	0.9554	40.54 ± 2.92	
22	150	15.624 ± 1.131	75.772 ± 9.028	4.85	0.9909	0.9555	33.4 ± 2.6	
23	150	15.353 ± 1.117	86.771 ± 11.62	5.65	0.9909	0.9555	32.84 ± 2.56	
24	150	17.133 ± 1.204	73.357 ± 12.197	4.28	0.9909	0.9555	36.44 ± 2.76	37.37 ± 4.44
Terrace T3i								
28	150	18.179 ± 1.314	73.916 ± 19.572	4.07	0.9909	0.9558	38.45 ± 2.98	38.45 ± 2.98
Terrace T2i								
29	140	17.35 ± 1.2	86.018 ± 10.346	4.96	0.9825	0.9558	37.13 ± 2.77	
30	140	15.679 ± 1.181	80.765 ± 10.841	5.15	0.9825	0.9558	33.78 ± 2.72	35.45 ± 2.37
Terrace T2d								
1	84	15.287 ± 0.561	84.65 ± 9.573	5.54	0.9367	0.9533	34.6 ± 1.6	
3	84	16.378 ± 0.586	102.963 ± 7.337	6.29	0.9367	0.9533	36.9 ± 1.68	
7	75	15.639 ± 0.547	91.353 ± 11.1	5.84	0.9295	0.9533	35.62 ± 1.6	
2	84	14.561 ± 1.702	91.357 ± 7.346	6.27	0.9367	0.9534	33.02 ± 3.97	
4	84	16.11 ± 1.857			0.9367	0.9534	36.34 ± 4.31	
5	84	16.315 ± 1.874	82.935 ± 6.668	5.08	0.9367	0.9533	36.77 ± 4.35	
6	80	15.919 ± 2.582	81.591 ± 8.387	5.13	0.9335	0.9533	36.06 ± 5.94	
8	75	14.984 ± 1.871	75.843 ± 14.617	5.06	0.9295	0.9534	34.2 ± 4.38	35.44 ± 1.37
Terrace T1								
50	30	7.253 ± 0.265	63.346 ± 7.857	8.73	0.8938	0.9534	17.52 ± 0.81	
51	30	4.576 ± 0.184	31.98 ± 5.048	6.99	0.8938	0.9532	11.08 ± 0.54	14.30 ± 4.56
52	30	15.679 ± 0.503	117.253 ± 14.841	7.48	0.8938	0.9534	37.02 ± 1.58	
Average = 5.48 ± 1.07								
Average T2 35.53 ± 2.48								

§ Mean is average of ^{10}Be age, and error is standard deviation.

* Not included in average calculation.